Earthquake in a Maze: Compressional Rupture Branching During the 2012 M_W 8.6 Sumatra Earthquake

L. Meng *et al.*

Science **337**, 724 (2012);
DOI: 10.1126/science.1224030

Science (print ISSN 0036-8075; online ISSN 1095-9203) is published weekly, except the last week in December, by the American Association for the Advancement of Science, 1200 New York Avenue NW, Washington, DC 20005.

Earthquake in a Maze: Compressional Rupture Branching During the 2012 M_w 8.6 Sumatra Earthquake

L. Meng,* J.-P. Ampuero, J. Stock, Z. Duputel, Y. Luo, V. C. Tsai

Seismological observations of the 2012 moment magnitude 8.6 Sumatra earthquake reveal unprecedented complexity of dynamic rupture. The surprisingly large magnitude results from the combination of deep extent, high stress drop, and rupture of multiple faults. Back-projection source imaging indicates that the rupture occurred on distinct planes in an orthogonal conjugate fault system, with relatively slow rupture speed. The east-southeast–west-northwest ruptures add a new dimension to the seismotectonics of the Wharton Basin, which was previously thought to be controlled by north-south strike-slip faulting. The rupture turned twice into the compressive quadrant, against the preferred branching direction predicted by dynamic Coulomb stress calculations. Orthogonal faulting and compressional branching indicate that rupture was controlled by a pressure-insensitive strength of the deep oceanic lithosphere.

The 11 April 2012 moment magnitude (M_w) 8.6 earthquake off shore of Sumatra is a record-breaking event in many respects. It is the largest strike-slip and intraplate earthquake ever recorded and, as shown here, one of the most complicated ruptures ever imaged by modern seismology. The faulting geometry and the peculiarities of its complex rupture path offer a rare opportunity to probe the mechanics of the oceanic lithosphere.

The earthquake occurred in the diffuse deformation zone between the Indian and Australian plates (Fig. 1, left, inset). Its focal mechanism is typical for the region (*1*), with *T* axis normal to the Sumatra subduction trench as observed for intraplate oceanic strike-slip earthquakes elsewhere (*2*) and consistent with regional stress modeling (*3*). The rupture initiated in the Paleogene oceanic lithosphere formed at the Wharton Basin spreading center but extended unimpeded into the adjacent oceanic lithosphere affected by later volcanism on the Ninetyeast Ridge (NER).

Because of the remote offshore location of this earthquake, geodetic constraints on fault geometry and static slip for teleseismic finite source inversions are unavailable. We imaged the rupture process by means of back-projection of teleseismic data from European and Japanese seismic networks. We applied the Multitaper-MUSIC array processing technique, which provides higher resolution than that of conventional beamforming (*4*). We also adopted a "reference window" strategy so as to avoid the systematic "swimming" artifact (*5*). High-frequency (HF, 0.5 to 1 Hz) source radiation is reliably imaged during 160 s (movies S1 and S2). The methods and their resolution and uncertainty analysis are described in the supplementary materials. The spatiotemporal evolution of the main HF sources (Figs. 1 and 2) is remarkably complex. The rupture involved at least three different, almost orthogonal, faults. Their strikes are consistent with the conjugate planes of centroid moment tensor (CMT) solutions and with the distribution of aftershocks (Fig. 1). The rupture process comprises at least three distinct stages (Fig. 1, right, inset), and the rupture length and speed on each fault are shown in Fig. 2. It started as a bilateral rupture on a fault striking WNW-ESE ("fault A") with a rupture length of ~100 km and duration of ~25 s. This stage generated the strongest HF radiation (fig. S3). The rupture then branched into an almost orthogonal fault ("fault B"), breaking bilaterally for ~60 s over 300 km. The onset of rupture to the NNE on fault B was delayed by ~15 s and then propagated until near the Sumatra trench. Fault B's SSW rupture front branched into a third almost orthogonal fault ("fault C"), which ruptured to the NNW for ~100 km. The final rupture stage involved stepping northward from fault C onto a parallel fault ("fault D") that crossed the NER. The total rupture length on faults A, B, and C is 500 km, which is half that obtained by the extrapolation of empirical scaling relations (*6*). Two hours later, the largest (M_w 8.2) aftershock initiated on the SSE continuation of fault C but ruptured bilaterally for ~100 km on an orthogonal fault (Fig. 1, right).

The magnitude of this earthquake is surprising in an intraplate environment characterized by relatively short faults with wide stepovers. With hindsight, the large magnitude of the 2012 Sumatra earthquake stems from a conjunction of circumstances: wide depth extent, high stress drop, and rupture of multiple faults. Reported centroid depths are below 25 km [U.S. Geological Survey (USGS) CMT/W-phase solution; Global Centroid-Moment-Tensor (GCMT)]. Rupture penetrating into the uppermost mantle is consistent with old and hence thick oceanic lithosphere (~55 million years old, ~35 km) (*7*). West of the NER, seismic reflection lines show faults cutting through the Moho discontinuity (*8*). Considering uniform slip in a 500-km-long and 40-km-deep rupture, the estimated average slip is ~15 m, and the stress drop is ~15 MPa, which is high but similar to the stress drop of other large oceanic strike-slip earthquakes (*9*, *10*) and not unusual for intraplate and subcrustal earthquakes (*11*, *12*). The multisegment rupture was encouraged by stressing from the M_w 9.1 2004 Sumatra megathrust earthquake, whose southernmost large-slip region coincides with the latitude of the 2012 event (Fig. 1, left). Coulomb stress calculations show that thrust-faulting favors slip on outer-rise strike-slip faults that are oblique to the trench (*13*).

The dominant E-W rupture of faults A, C, and D adds a new dimension to the prevailing view of the seismotectonics of this region. These faults are subparallel to long-lived but still active faults on the NER (Fig. 3) (*14*). The bisecting direction of the conjugate faults is consistent with the orientation of the principal stress inferred from seismic and GPS data (*15*). Strike-slip focal mechanisms from the zone east of the NER have previously been attributed to slip on N-S–striking faults, such as those imaged in seismic lines south of the equator in the Wharton Basin (*16*). Active E-W–striking faults west of the NER are generally attributed to compressional deformation (*8*). The rupture geometry of this earthquake indicates that active E-W right-lateral faults are also an important part of the kinematics of this broad deformation zone.

Back-projection imaging reveals rupture on almost orthogonal faults, as confirmed with back-projection of the M_w 8.2 aftershock. This has been observed in earthquake pairs (such as 1987 M_w 6.2 Superstition Hills and M_w 6.7 Elmore Ranch; and 1992 M_w 7.3 Landers and M_w 6.5 Big Bear) but only rarely during single events, such as in the 13 May 1997 M_w 6 Kagoshima earthquake (*17*) and in the 2000 M_w 7.8 Wharton Basin earthquake (*9*), although orthogonal faulting of the latter is not confirmed by later studies (*18*). A multiple CMT inversion (methods are available in the supplementary materials) yields two subevents with similar mechanisms; the second one was ~200 km SW of the hypocenter (Fig. 1, left), which is consistent with rupture on the SSW branch of fault B and on fault C. In the crust, conjugate shear faults intersect at an angle of ~60°. The seafloor magnetic patterns (Fig. 1, right) rule out reactivation of fossil systems of transform faults and ridges. The wide angle between these faults requires pressure-insensitive strength during their formation (Fig. 2, inset).

The rupture path of this earthquake is unexpected: In two occasions, the rupture branched preferably into the compressive (strengthened) quadrant, with arrest or delay in the alternative branch. The NNW-ward rupture front on the right-lateral fault A first turned left into the SSW segment of fault B. Rupture on the NNE segment of fault B was delayed by ~15 s. This behavior is mirrored by the second branching episode. The SSW-ward rupture front on the

Seismological Laboratory, Division of Geological and Planetary Sciences, California Institute of Technology, Pasadena, CA 91125, USA.

*To whom correspondence should be addressed. E-mail: lsmeng@gps.caltech.edu

left-lateral fault B turned right into the NNW segment of fault C. In both cases, the preferred branching direction is toward the compressive quadrant of the previous segment, which is opposite to the expectation based on usual values of friction coefficient. Analysis of the dynamic stresses induced near the tip of a right-lateral crack on orthogonal left-lateral faults (Fig. 2, right) shows that the observed branching direction requires two circumstances: low rupture speed ($\frac{V_r}{V_s} \sim 0.5$, where V_r is the rupture speed and V_s is the shear-wave speed) and low apparent friction coefficient (~0.2)—a small slope of the failure envelope in a shear-versus-normal stress diagram (Fig. 2, inset). The former is robustly supported by our back-projection results: The overall rupture speed is ~2.5 km/s on faults A and B (Fig. 2, left), which is not unusual compared with global average values but is slow compared with wave speeds below the oceanic Moho (50 to 60% of *S* wave speed) (*19*). The latter implies a pressure-insensitive strength, which is characteristic of ductile materials at depth. An alternative explanation by poroelastic effects (*20*) with large Skempton's coefficient requires high fluid pressure that is inconsistent with the large stress drop.

Sustained seismic rupture also requires a dynamic weakening mechanism. The relatively slow rupture speed suggests scale-dependent energy dissipation by the rupture process. The ductile shear heating instability proposed by (*21*, *22*) operates between 600 and 800°C, which is limited to a roughly 40 to 60 km depth. Serpentinized peridotite has low pressure sensitivity at confining pressures over few 100 MPa, with apparent friction coefficients as low as 0.15 (*23*), and might dynamically weaken by dehydration embrittlement (*24*). However, the serpentinization reaction is possible only up to 400 to 500°C, which corresponds to ~25 km depth (*8*). A single dynamic weakening mechanism that can operate over the whole depth range of slip of this earthquake remains to be identified.

This is not the first time an earthquake has grown larger than expected or has occurred where it is least expected. The destructive 2011 M_w 9.0 Tohoku-Oki and M_w 6.3 Christchurch earthquakes illustrate the scientific challenge of estimating the likelihood of extreme events based on a short and incomplete historical record. The 2012 Sumatra earthquake raises the concern of similarly large events in continental strike-slip fault systems, which pose a higher hazard to populations. Although the tectonic setting in an oceanic intraplate zone of high deformation is rare, at least one of the ingredients that made this earthquake big—its large stress drop—is a general feature of other intraplate earthquakes (*11*). Its rupture complexity highlights the importance of considering earthquake scenarios with multisegment ruptures. The rupture transition from faults C and D across an offset larger than 20 km is particularly extreme (*25*). The relation to the 2004 Sumatra earthquake suggests that large outer-rise events induced by megathrust events—although not producing damaging shaking because of their remote off-shore location—can pose a tsunami hazard if they have a dip component (*26*) or displace high topography (*27*). The Gorda plate in the southern Cascadia subduction zone is such an example.

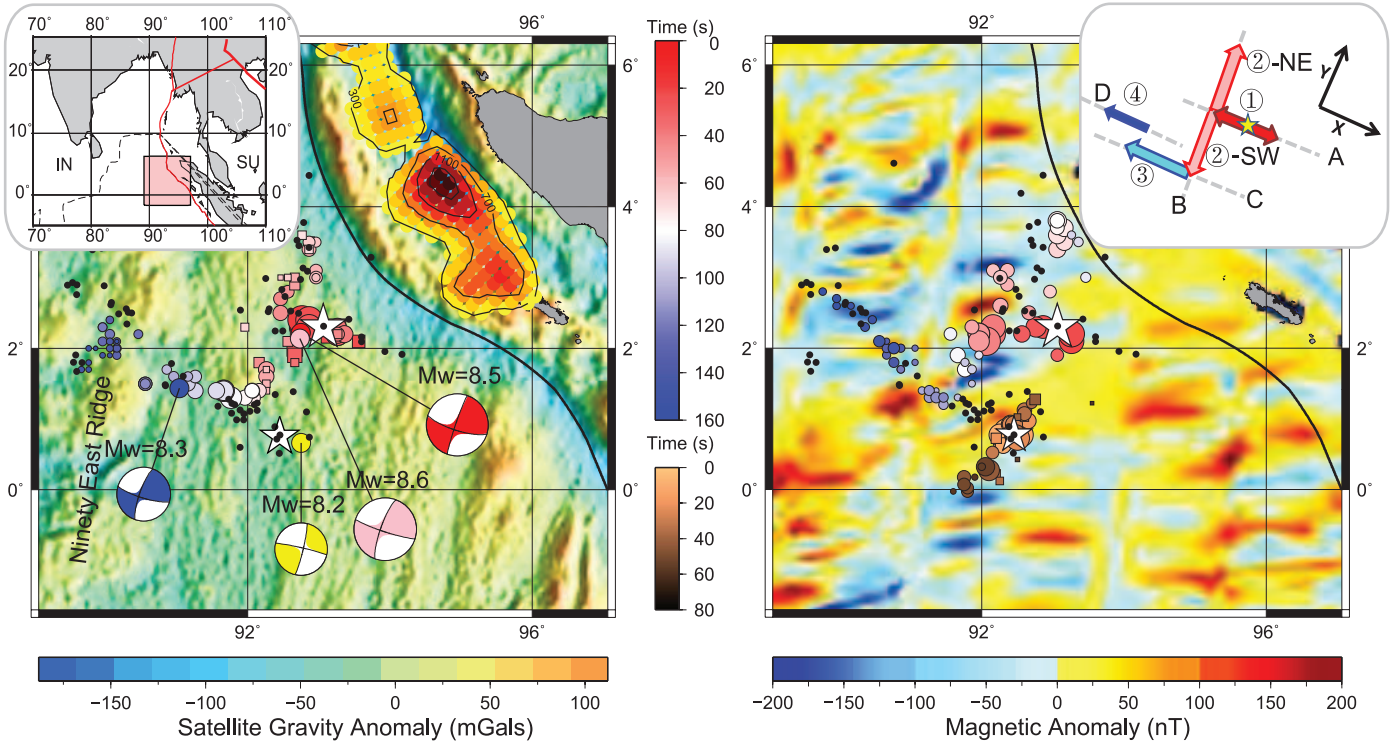

Fig. 1. Spatiotemporal distribution of HF radiation imaged by the (**left**) European and (**right**) Japanese networks. Colored circles and squares indicate the positions of primary and secondary peak HF radiation (from movies S1 and S2, respectively). Their size is scaled by beamforming amplitude, and their color indicates timing relative to hypocentral time (color scale in center). The secondary peaks of the MUSIC pseudo-spectrum are those at least 50% as large as the main peak in the same frame. The brown shaded circles in the right figure are the HF radiation peaks from the M_w 8.2 aftershock observed from Japan. The colored contours in the Sumatra subduction zone (left) represent the slip model of the 2004 M_w 9.1 Sumatra earthquake (*28*). The figure background is colored by the satellite gravity anomaly (left) in milligalileos (mgals) (color scale on bottom left) and the magnetic anomaly (right) in nanoteslas (color scale on bottom right). Black dots are the epicenters of the first day of aftershocks from the U.S. National Earthquake Information Center catalog. The big and small white stars indicate the hypocenter of the mainshock and M_w 8.2 aftershock. The moment tensors of the M_w 8.6 mainshock, M_w 8.2 aftershock, and double CMT solutions of the mainshock are shown as colored pink, yellow, red, and blue beach balls. The red line in the top left inset shows the boundary between the India (IN) and Sundaland (SU) plates (*29*). The patterned pink area is the diffuse deformation zone between the India and Australia plate. The red rectangular zone indicates the study area. The top right inset shows the interpreted fault planes (gray dashed lines) and rupture directions (colored arrows).

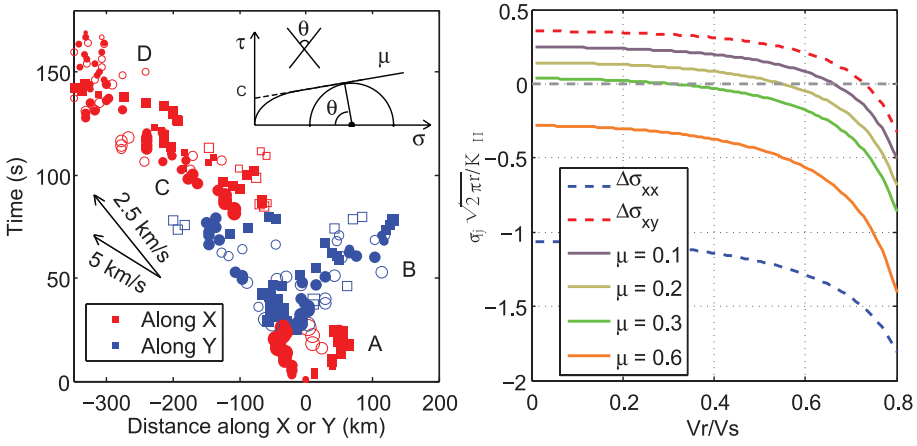

Fig. 2. Spatiotemporal details of the rupture process. (**Left**) Timing and position of the HF radiators relative to the hypocenter. The position is reported in alternation along the axes labeled X (red) and Y (blue) in Fig. 1, inset. Circles and squares are the results of Europe and Japan arrays, respectively. Solid and open symbols indicate principal and secondary HF radiators, respectively. (Inset) Shear strength (τ) versus normal stress (σ) diagram of a nonlinear strength envelope with small apparent friction coefficient μ (almost pressure-insensitive material) and large cohesion C, resulting in almost orthogonal failure planes (θ ~ 90°). (**Right**) Dynamic Coulomb stress changes induced near the tip of a right-lateral crack propagating at steady rupture speed, resolved onto orthogonal left-lateral faults in the compressional quadrant as a function of the ratio between rupture speed and shear-wave speed (V_r/V_s) (*30*). The symbols denote dynamic changes of normal stress ($\Delta\sigma_{xx}$, negative compressive, blue dashed line), shear stress ($\Delta\sigma_{xy}$, positive left-lateral, red dashed line), and Coulomb stress ($\Delta\sigma_{xy} + \mu\Delta\sigma_{xx}$, color solid curves, assuming various apparent friction coefficients μ indicated in the legend). Stresses are normalized based on the Mode II stress intensity factor (K_{II}) and the distance to the crack tip (r). Rupture on the compressive side can be triggered (positive Coulomb stress change) only for low enough apparent friction and rupture speed.

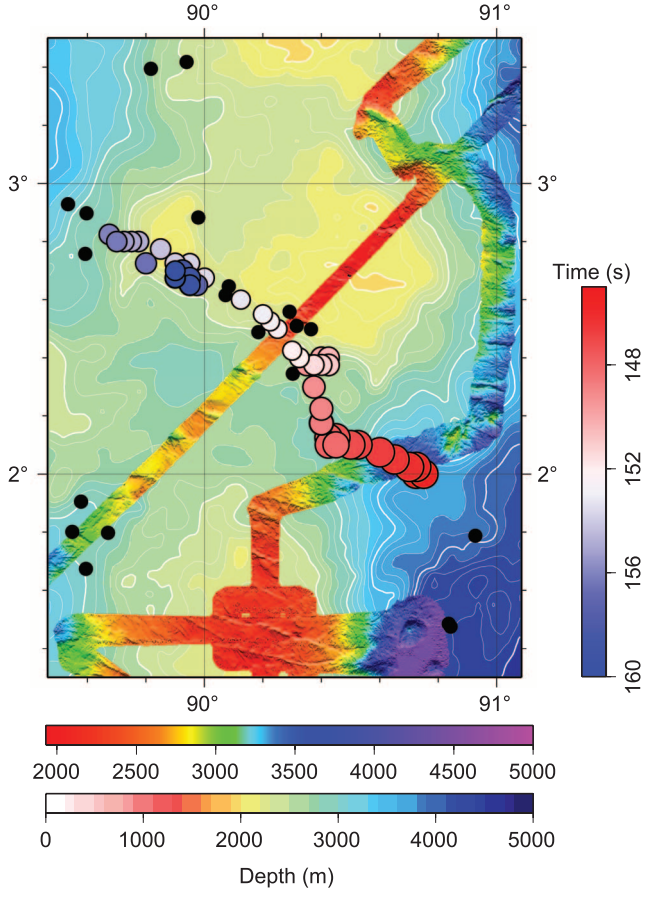

Fig. 3. Bathymetry where the rupture crosses the NER. Colored background is global bathymetry from SRTM30+ overlain by multibeam bathymetry from cruise KNOX06RR and cruise DYNAMO, respectively. Black dots indicate aftershocks, and circles indicate HF source radiators. These indicate rupture through the NER during the last 15 s of the earthquake. The rupture plane is consistent with numerous fault scarps visible in the multibeam bathymetry.

References and Notes

1. E. R. Engdahl, A. Villasenor, H. R. DeShon, C. H. Thurber, *Bull. Seismol. Soc. Am.* **97**, S43 (2007).
2. G. L. Choy, A. McGarr, *Geophys. J. Int.* **150**, 506 (2002).
3. S. Cloetingh, R. Wortel, *Tectonophysics* **132**, 49 (1986).
4. L. Meng, A. Inbal, J. P. Ampuero, *Geophys. Res. Lett.* **38**, L00G07 (2011).
5. L. Meng, J. P. Ampuero, Y. Luo, W. Wu, S. Ni, *Earth Planets Space* 10.5047/eps.2012.05.010 (2012).
6. D. L. Wells, K. J. Coppersmith, *Bull. Seismol. Soc. Am.* **84**, 974 (1994).
7. D. A. Wiens, S. Stein, *J. Geophys. Res.* **88**, 6455 (1983).
8. M. Delescluse, N. Chamot-Rooke, *Earth Planet. Sci. Lett.* **276**, 140 (2008).
9. D. P. Robinson, C. Henry, S. Das, J. H. Woodhouse, *Science* **292**, 1145 (2001).
10. M. Antolik, A. Kaverina, D. S. Dreger, *J. Geophys. Res. Solid Earth* **105**, 23825 (2000).
11. B. P. Allmann, P. M. Shearer, *J. Geophys. Res.* **114**, B01310 (2009).
12. A. Oth, D. Bindi, S. Parolai, D. Di Giacomo, *Geophys. Res. Lett.* **37**, L19304 (2010).
13. J. C. Rollins, R. S. Stein, *J. Geophys. Res.* **115**, B12306 (2010).
14. W. W. Sager *et al.*, *Geophys. Res. Lett.* **37**, L17304 (2010).
15. M. Delescluse, N. Chamotrooke, *Geophys. J. Int.* **168**, 818 (2007).
16. C. Deplus *et al.*, *Geology* **26**, 131 (1998).
17. H. Horikawa, *Bull. Seismol. Soc. Am.* **91**, 112 (2001).
18. R. E. Abercrombie, M. Antolik, G. Ekstrom, *J. Geophys. Res.* **108**, (B1), 2018 (2003).
19. F. Klingelhoefer *et al.*, *J. Geophys. Res.* **115**, B01304 (2010).
20. M. Cocco, J. R. Rice, *J. Geophys. Res.* **107**, 2030 (2002).
21. P. B. Kelemen, G. Hirth, *Nature* **446**, 787 (2007).
22. J. J. McGuire, G. C. Beroza, *Science* **336**, 1118 (2012).
23. J. Escartín, G. Hirth, B. Evans, *Geology* **29**, 1023 (2001).
24. H. Jung, H. W. Green II, L. F. Dobrzhinetskaya, *Nature* **428**, 545 (2004).
25. S. G. Wesnousky, *Nature* **444**, 358 (2006).
26. T. Lay, C. J. Ammon, H. Kanamori, M. J. Kim, L. Xue, *Earth Planets Space* **63**, 713 (2011).
27. Y. Tanioka, K. Satake, *Geophys. Res. Lett.* **23**, 861 (1996).
28. M. Chlieh *et al.*, *Bull. Seismol. Soc. Am.* **97**, S152 (2007).
29. C. DeMets, R. G. Gordon, D. F. Argus, *Geophys. J. Int.* **181**, 1 (2010).
30. A. N. B. Poliakov, R. Dmowska, J. R. Rice, *J. Geophys. Res.* **107**, 2295 (2002).

Acknowledgments: This research was supported by NSF grant EAR-1015704, by the Gordon and Betty Moore Foundation, and by the Southern California Earthquake Center (SCEC), which is funded by NSF Cooperative Agreement EAR-0106924 and USGS Cooperative Agreement 02HQAG0008. The Japanese Hi-net (www.hinet.bosai.go.jp) and the European ORFEUS (www.orfeus-eu.org) data centers were used to access the broadband seismograms. The magnetic anomalies are from the EMAG2 database available at the National Geophysical Data Center (www.ngdc.noaa.gov). The satellite gravity anomaly data are from the UCSD TOPEX v. 18.1 database. The multibeam bathymetry from the KNOX06RR cruise is available at Marine Geoscience Data System (www.marine-geo.org). We thank R.-C. Lien and B. Ma for providing the Roger Revelle (RR1201) multibeam data from the DYNAMO cruise. We thank H. Kanamori for valuable discussions about this event. This paper is Caltech Tectonics Observatory contribution 215, Caltech Seismo Lab contribution 10078, and SCEC contribution 1656.

Supplementary Materials

www.sciencemag.org/cgi/content/full/science.1224030/DC1
Materials and Methods
Figs. S1 to S8
References (*31*–*36*)
Movies S1 and S2

30 April 2012; accepted 5 July 2012
Published online 19 July 2012;
10.1126/science.1224030

Supplementary Material for

Earthquake in a Maze: Compressional Rupture Branching During the 2012 M_w 8.6 Sumatra Earthquake

L. Meng,* J.-P. Ampuero, J. Stock, Z. Duputel, Y. Luo, V. C. Tsai

*To whom correspondence should be addressed. E-mail: lsmeng@gps.caltech.edu

Published 19 July 2012 on *Science* Express
DOI: 10.1126/science.1224030

This PDF file includes:

Other Supplementary Material for this manuscript includes the following:
(available at www.sciencemag.org/cgi/content/full/science.1224030/DC1)

Movies S1 and S2

Materials and Methods

Back-projection data selection and processing:

We processed the seismic data recorded by various seismic arrays at epicentral distances between 30 and 90 degrees. The large aperture and dense spacing of the European (www.orfeus-eu.org; Figure S1) and Japanese Hi-net networks (www.hinet.bosai.go.jp; Figure S2) provided fine spatial resolution for this event. The two arrays are located at almost orthogonal azimuths relative to the source area, providing complementary views of the rupture process. The P waveforms were filtered between 0.5 and 1 Hz, selected by their signal-to-noise ratio and by the mutual coherency of their initial 10 seconds, and then aligned by multi-channel cross-correlation. We applied the MUSIC back-projection technique (*4*, *31*) on sliding windows ten seconds in length. This source imaging technique allows tracking the migration of the multiple sources of high-frequency (HF) radiation of an earthquake rupture. Our particular approach combines a high-resolution array processing technique (*32*, *33*) with multi-taper cross-spectral estimation (*34*) to achieve higher resolution than conventional beamforming. Adopting a "reference window" strategy avoids the systematic "swimming" artifact (*5*). The MUSIC pseudo-spectrum is back-projected into the off-Sumatra region based on P travel times computed by the Tau-P toolkit and the IASP91 model (*36*)

Multiple point source analysis:

Seismic waves from the 2012 Sumatra earthquake sequence were recorded by a large number of broadband seismic stations enabling robust and reliable characterization of the overall source characteristics at long periods. For the Mw=8.6 event, 113 channels were used to perform a multiple point source inversion. We inverted simultaneously for the moment tensors of the subevents, their locations (latitude, longitude, depth) and time delays using a global sampling approach. The inversion is performed using the W-phase waveforms at shorter period (150-500 s) than the usual practice for single point source inversions of Mw>8.0 earthquakes. The optimal centroid depth of the mainshock is 30 km. Our preferred model is a two point source solution which is presented on Fig. 1.

Resolution and uncertainty of back-projection source imaging:

We conducted several analyses to understand the strengths and limitations of our back-projection method, as specifically applied to the European and Japanese arrays. We address two different array performance criteria. The spatial *resolution* of an array is defined as the capability to separate two simultaneous sources of different location: the *resolution length* is the minimum distance between sources that can be distinguished without ambiguity. The spatial *uncertainty* of an array is defined as the error in estimates of source location for isolated sources.

The resolution length that can be achieved with linear beamforming is conventionally estimated as the width at half peak amplitude of the main lobe of the array response function (ARF, *35*). Figs. S4 and S5 show the ARFs of the Japanese and the European networks back-projected into the off-Sumatra region. The European ARF is relatively

compact with resolution lengths of 35 km in the N-S direction and 65 km in the E-W direction. These are one order of magnitude smaller than the source dimension of the M8.6 off-Sumatra event, which indicates that the overall rupture process can be resolved as long as there is adequate signal coherence. The Japanese Hi-Net array has a larger and more anisotropic ARF, with resolution lengths of 450 km in the N-S direction and 70 km in the E-W direction. This helps explaining why the early separation of the bilateral rupture fronts on fault B is imaged by the European array (movie S2) but the two fronts appear simultaneously in the Hi-Net images only when they reach the ends of fault B.

In back-projection source imaging with linear beamforming, the estimation of source location is based on identifying the peak position of an image that is smeared by the array response. The Cramer-Rao bound, a theoretical estimate of the upper bound of uncertainty of an estimator, indicates that the source location uncertainty is proportional to the resolution length of the ARF and inversely proportional to the signal-to-noise ratio of the images (SNR), defined as the ratio between the main peak amplitude and the mean amplitude of the background peaks of the image. The SNR depends on both the signal quality (noise and multipath) and the station density (sidelobe amplitude). The Hi-Net array has a particularly large SNR due to its small ambient noise level (borehole stations) and extremely dense spacing (~20 km).

However, due to the nonlinearity of the MUSIC technique, its resolution cannot be fully appreciated by considering the ARF. Typically, the resolution length of MUSIC is at least two times smaller than the beamforming resolution length (*31*). Moreover, the resolution analysis based on the ARF assumes perfect signal coherence. In practice, we quantify the uncertainty of back-projection of Hi-Net data by bootstrapping the back-projection of a M6.1 aftershock that occurred on April 21th, 2012 at 93.39 degree E and 2.22 degree N. The aftershock seismograms are first aligned by the initial 3 s of the P-wave arrival. The noise at each station is computed as the waveform residual with respect to the array-stacked waveform. The noise is shuffled by randomizing its Fourier phase spectrum, then added back to the stack. One thousand synthetic realizations of the aftershock array recordings plus noise are then back-projected considering the 10-s long window that begins at the initial arrival. The resulting back-projection locations are shown in Fig. S6. The bootstrap 95% confidence ellipse is elongated along the N-S direction with a major axis length of 9.5 km and minor axis length of 2.8 km. Unfortunately, the recording of this aftershock at the European array is too weak to be used in the 0.5-1 Hz frequency band.

To further understand the performance of the back-projection on complicated ruptures, we conduct two synthetic earthquake scenarios. To include key characteristics of the real wavefield, such as the decay of waveform coherence as a function of time, we use the M6.1 event as empirical Green's function. Inspired by our final back-projection result, particularly a jump from the fault C to fault D imaged with the Hi-Net array, we test scenarios of bilateral rupture on Fault A and B and unilateral rupture on Fault C with (Fig.S7) or without (Fig.S8) an additional fault D. We consider a uniform distribution of sub-sources, regularly located every 15 km along each fault. The rupture times correspond to an assumed rupture speed of 2.5 km/s. The MUSIC back-projection

technique recovers the location and timing of the scenario sources very well. The uncertainty of the peak locations is less than 20 km, which is reasonably good considering the coda and interference between sub-sources. These synthetic tests indicate that the jump between faults C and D is resolvable by the Hi-Net array.

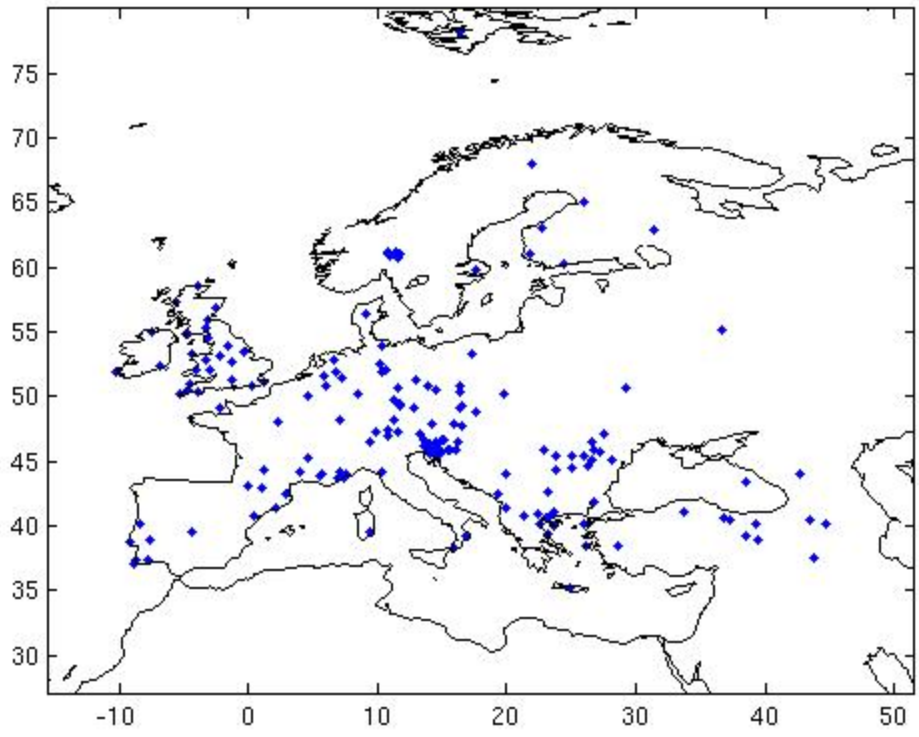

Fig. S1
Selected stations used for back-projection from the European network.

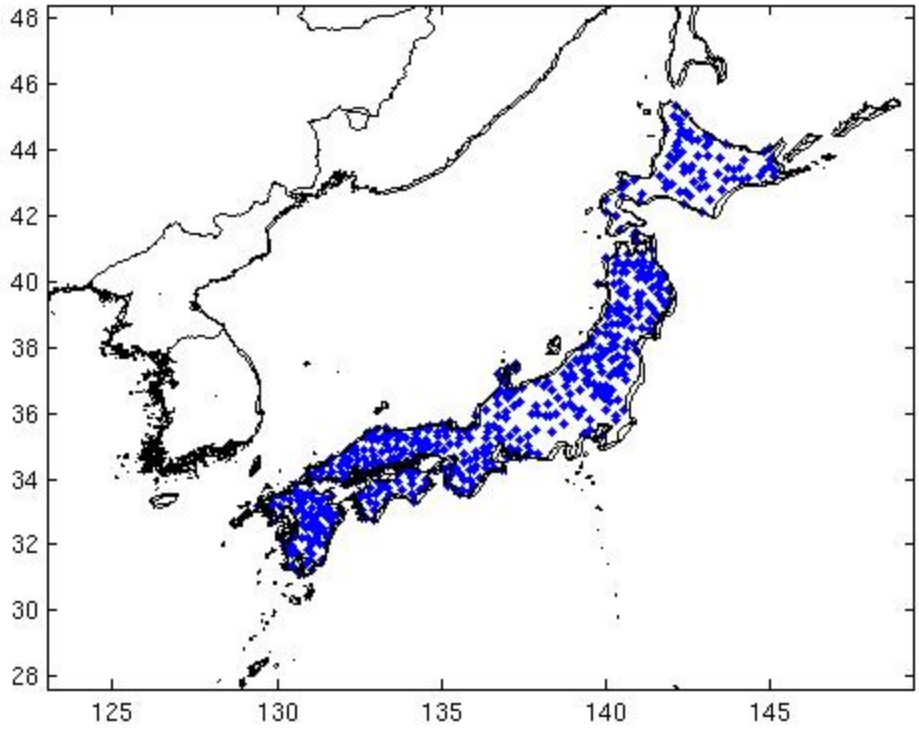

Fig. S2
Selected stations for back-projection from the Hi-Net (Japan) network.

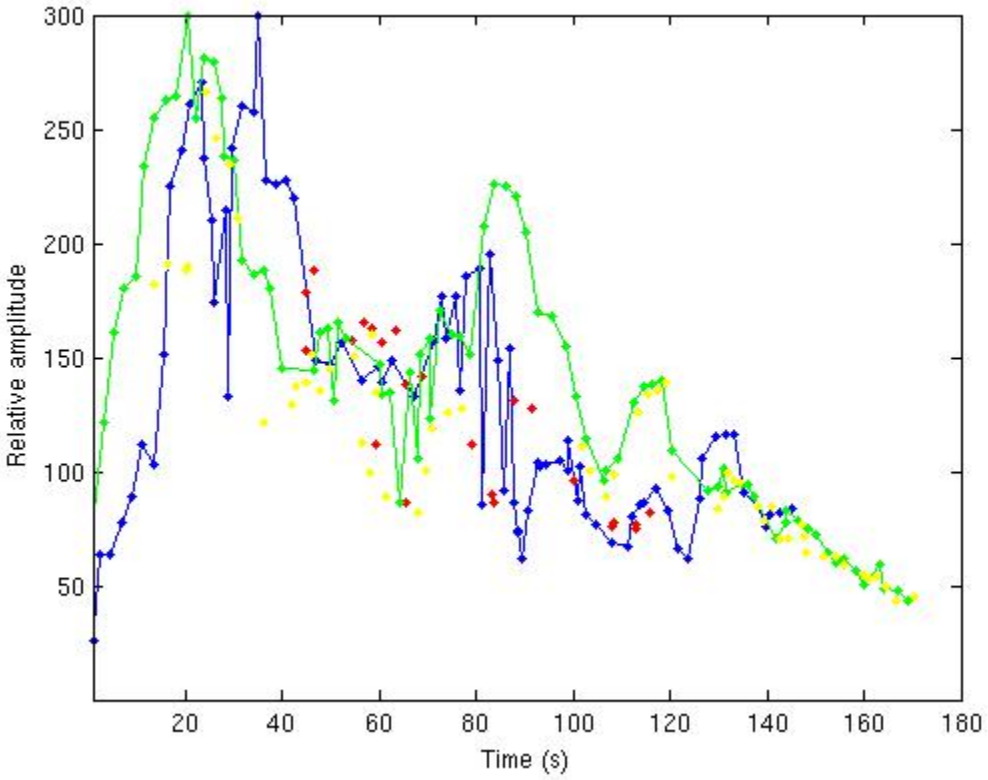

Fig. S3

Beamforming source amplitude evaluated at the location of the HF radiators obtained by MUSIC as a function of time, obtained with the European array (green) and Japanese Hi-Net array (blue). The scale is normalized by the beamforming amplitude of the initial window. The yellow and red dots indicate the amplitude of the secondary sources for the European and Japanese arrays, respectively.

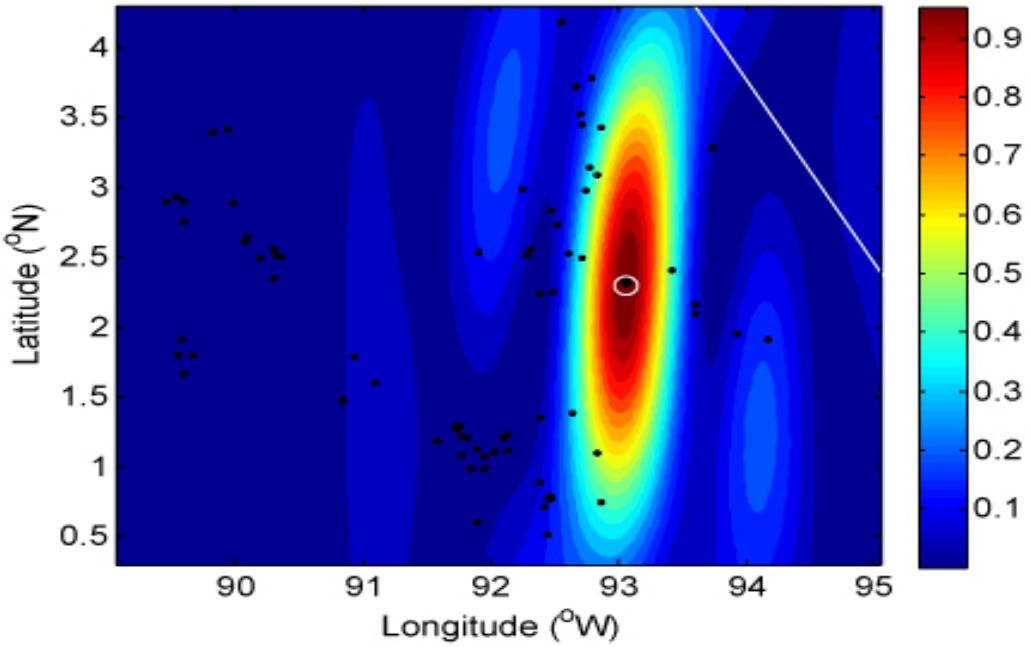

Fig. S4

Array response pattern of the Japanese Hi-Net array back-projected into the off-Sumatra earthquake region, plotted in map view. The color scale indicates the power of the array response, normalized by its peak value. The white line denotes the trace of the Sumatra trench. The white circle is the location of the epicenter. The black dots are early aftershocks that occurred within 24 hours of the mainshock.

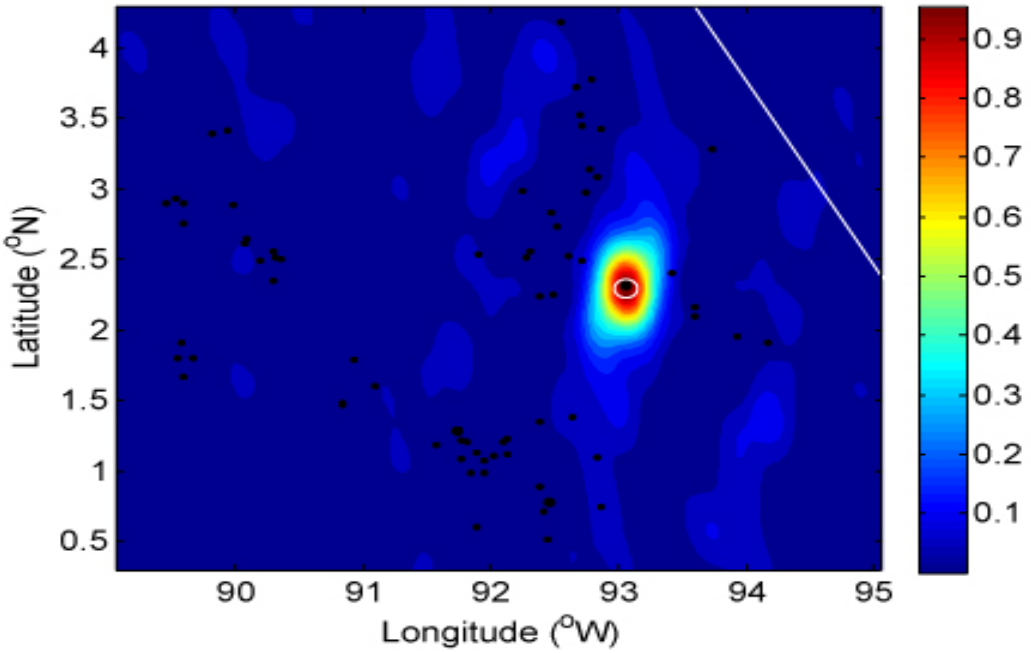

Fig. S5

Array response pattern of the European network. The convention is the same as in the previous figure.

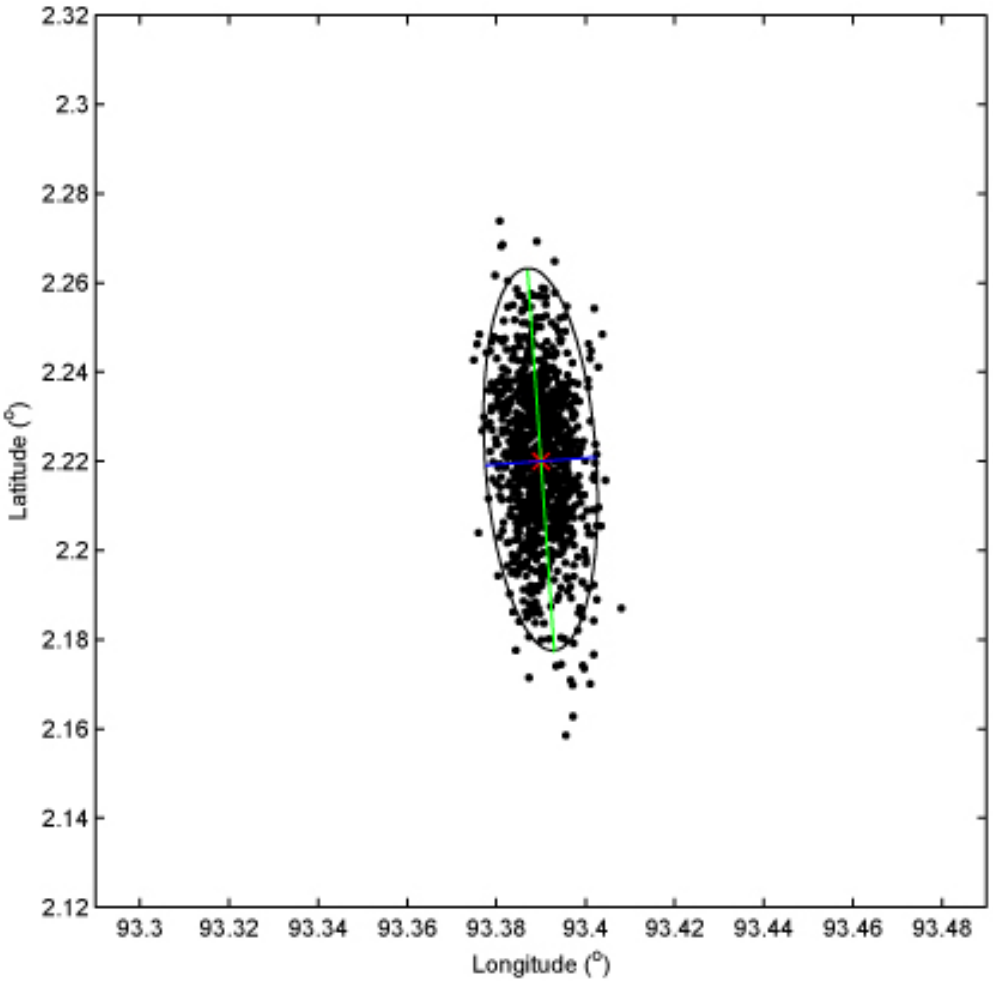

Fig. S6

Uncertainty of the back-projection. A M6.1 aftershock that occurred on April 21th, 2012 is used here as an empirical Green's function. The red asterisk denotes the hypocenter. The black dots are the back-projection of the bootstrapped aftershock recordings. The ellipse is the 95% confidence interval. It has a 9.5 km long major axis (blue line) and 2.8 km long minor axis (green line).

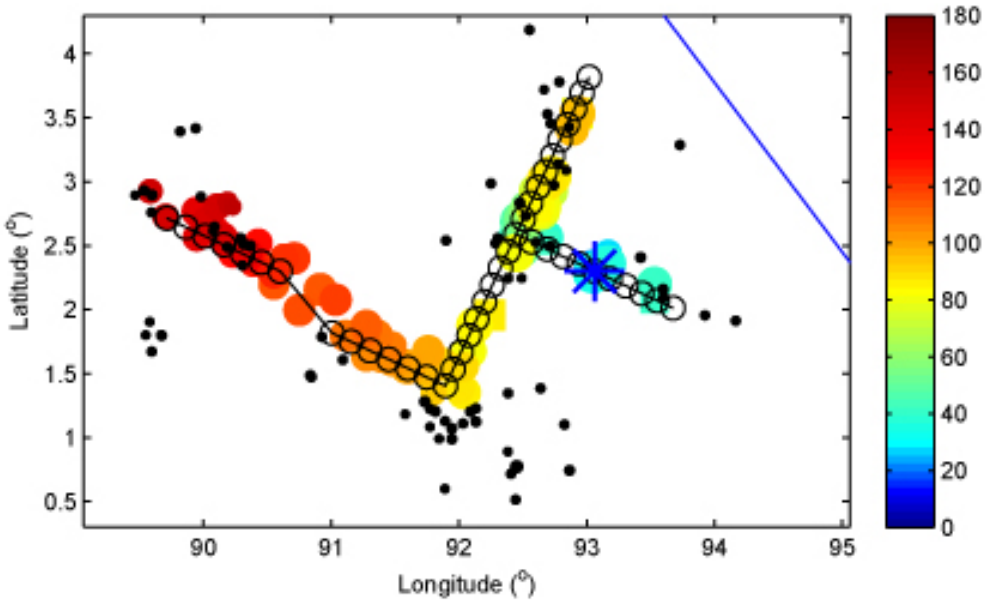

Fig. S7

Back-projection of a synthetic rupture scenario. The black circles are the synthetic sources. The colored circles are the recovered back-projection locations color-coded by time. The black dots are the early aftershocks that occurred within 24 hours of the mainshock.

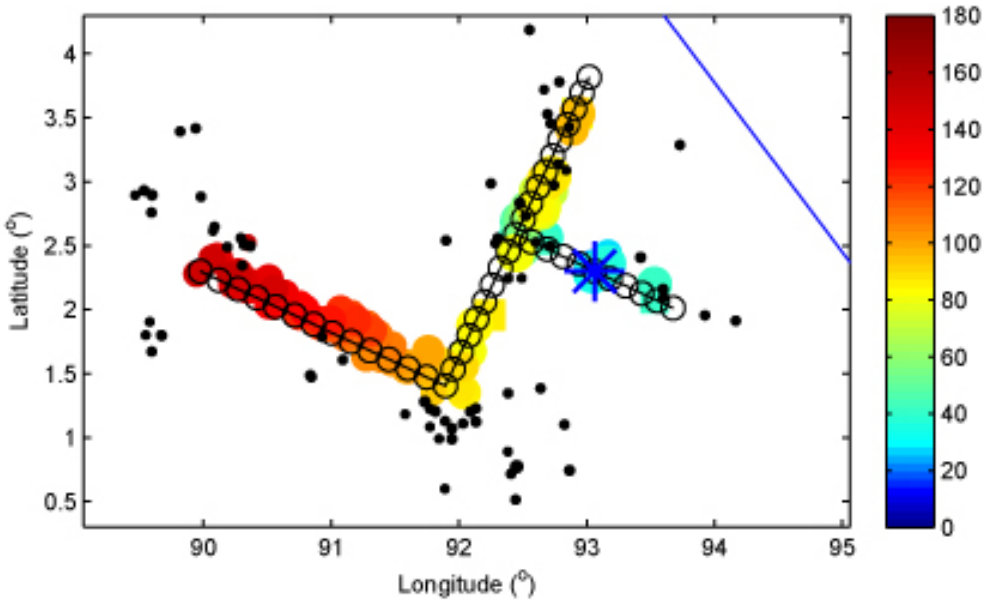

Fig. S8

Back-projection of a synthetic rupture scenario without offset between faults C and D. The convention of the figure is the same as in the previous one.

Movie S1

The movie shows the raw results of back-projection source imaging based on teleseismic data from European networks. Warm colors indicate the positions of the high frequency (0.5 to 1 Hz) radiation back-projected onto the source region based on IASP91 travel times (*36*). The sliding window is 10-s long and the origin time is 08:38:37, 04-12-12 (UTC). The beginning of the sliding window is set to be 5 s before the initial P-wave arrival. Colors indicate the amplitude of the MUSIC pseudo-spectrum on a logarithmic scale (dB) after subtracting the background level and rescaling the maximum to the linear beamforming power in each frame separately. The white star is the mainshock epicenter and the green circles are the epicenters of the first day of aftershocks from the NEIC catalog. Time relative to hypocentral arrival time is shown on top. The trench and coastlines are shown by white curves.

Movie S2

Back-projection source imaging based on teleseismic data from Japanese networks. Same convention as the previous movie.

References and Notes

1. E. R. Engdahl, A. Villasenor, H. R. DeShon, C. H. Thurber, Teleseismic relocation and assessment of seismicity (1918-2005) in the region of the 2004 Mw 9.0 Sumatra-Andaman and 2005 Mw 8.6 Nias Island great earthquakes. *Bull. Seismol. Soc. Am.* **97**, (1A), S43 (2007). doi:10.1785/0120050614

2. G. L. Choy, A. McGarr, Strike-slip earthquakes in the oceanic lithosphere: observations of exceptionally high apparent stress. *Geophys. J. Int.* **150**, 506 (2002). doi:10.1046/j.1365-246X.2002.01720.x

3. S. Cloetingh, R. Wortel, Stress in the Indo-Australian Plate. *Tectonophysics* **132**, 49 (1986). doi:10.1016/0040-1951(86)90024-7

4. L. Meng, A. Inbal, J. P. Ampuero, A window into the complexity of the dynamic rupture of the 2011 Mw 9 Tohoku-Oki earthquake. *Geophys. Res. Lett.* **38**, L00G07 (2011). doi:10.1029/2011GL048118

5. L. Meng, J. P. Ampuero, Y. Luo, W. Wu, S. Ni, Mitigating Artifacts in Back-Projection Source Imaging with Implications on Frequency-Dependent Properties of the Tohoku-Oki Earthquake. *Earth Planets Space* 10.5047/eps.2012.05.010 (2012).

6. D. L. Wells, K. J. Coppersmith, New Empirical Relationships among Magnitude, Rupture Length, Rupture Width, Rupture Area, and Surface Displacement. *Bull. Seismol. Soc. Am.* **84**, 974 (1994).

7. D. A. Wiens, S. Stein, Age Dependence of Oceanic Intraplate Seismicity and Implications for Lithospheric Evolution. *J. Geophys. Res.* **88**, (B8), 6455 (1983). doi:10.1029/JB088iB08p06455

8. M. Delescluse, N. Chamot-Rooke, Serpentinization pulse in the actively deforming Central Indian Basin. *Earth Planet. Sci. Lett.* **276**, 140 (2008). doi:10.1016/j.epsl.2008.09.017

9. D. P. Robinson, C. Henry, S. Das, J. H. Woodhouse, Simultaneous rupture along two conjugate planes of the Wharton Basin earthquake. *Science* **292**, 1145 (2001). doi:10.1126/science.1059395 Medline

10. M. Antolik, A. Kaverina, D. S. Dreger, Compound rupture of the great 1998 Antarctic plate earthquake. *J. Geophys. Res. Solid Earth* **105**, (B10), 23825 (2000). doi:10.1029/2000JB900246

11. B. P. Allmann, P. M. Shearer, Global variations of stress drop for moderate to large earthquakes. *J. Geophys. Res.* **114**, (B1), B01310 (2009). doi:10.1029/2008JB005821

12. A. Oth, D. Bindi, S. Parolai, D. Di Giacomo, Earthquake scaling characteristics and the scale-(in)dependence of seismic energy-to-moment ratio: Insights from KiK-net data in Japan. *Geophys. Res. Lett.* **37**, L19304 (2010). doi:10.1029/2010GL044572

13. J. C. Rollins, R. S. Stein, Coulomb stress interactions among M >= 5.9 earthquakes in the Gorda deformation zone and on the Mendocino Fault Zone, Cascadia subduction zone, and northern San Andreas Fault. *J. Geophys. Res.* **115**, (B12), B12306 (2010). doi:10.1029/2009JB007117

14. W. W. Sager *et al*., Large fault fabric of the Ninetyeast Ridge implies near-spreading ridge formation. *Geophys. Res. Lett.* **37**, L17304 (2010). doi:10.1029/2010GL044347

15. M. Delescluse, N. Chamotrooke, Instantaneous deformation and kinematics of the India-Australia Plate. *Geophys. J. Int.* **168**, 818 (2007). doi:10.1111/j.1365-246X.2006.03181.x

16. C. Deplus *et al*., Direct evidence of active deformation in the eastern Indian oceanic plate. *Geology* **26**, 131 (1998). doi:10.1130/0091-7613(1998)026<0131:DEOADI>2.3.CO;2

17. H. Horikawa, Earthquake doublet in Kagoshima, Japan: Rupture of asperities in a stress shadow. *Bull. Seismol. Soc. Am.* **91**, 112 (2001). doi:10.1785/0119990131

18. R. E. Abercrombie, M. Antolik, G. Ekstrom, The June 2000 M-w 7.9 earthquakes south of Sumatra: Deformation in the India-Australia Plate. *J. Geophys. Res.* **108**, (B1), 2018 (2003). doi:10.1029/2001JB000674

19. F. Klingelhoefer *et al*., Limits of the seismogenic zone in the epicentral region of the 26 December 2004 great Sumatra-Andaman earthquake: Results from seismic refraction and wide-angle reflection surveys and thermal modeling. *J. Geophys. Res.* **115**, (B1), B01304 (2010). doi:10.1029/2009JB006569

20. M. Cocco, J. R. Rice, Pore pressure and poroelasticity effects in Coulomb stress analysis of earthquake interactions. *J. Geophys. Res.* **107**, (B2), 2030 (2002). doi:10.1029/2000JB000138

21. P. B. Kelemen, G. Hirth, A periodic shear-heating mechanism for intermediate-depth earthquakes in the mantle. *Nature* **446**, 787 (2007). doi:10.1038/nature05717 Medline

22. J. J. McGuire, G. C. Beroza, Geophysics. A rogue earthquake off Sumatra. *Science* **336**, 1118 (2012). doi:10.1126/science.1223983 Medline

23. J. Escartín, G. Hirth, B. Evans, Strength of slightly serpentinized peridotites: Implications for the tectonics of oceanic lithosphere. *Geology* **29**, 1023 (2001). doi:10.1130/0091-7613(2001)029<1023:SOSSPI>2.0.CO;2

24. H. Jung, H. W. Green, II, L. F. Dobrzhinetskaya, Intermediate-depth earthquake faulting by dehydration embrittlement with negative volume change. *Nature* **428**, 545 (2004). doi:10.1038/nature02412 Medline

25. S. G. Wesnousky, Predicting the endpoints of earthquake ruptures. *Nature* **444**, 358 (2006). doi:10.1038/nature05275 Medline

26. T. Lay, C. J. Ammon, H. Kanamori, M. J. Kim, L. Xue, Outer trench-slope faulting and the 2011 M(w) 9.0 off the Pacific coast of Tohoku Earthquake. *Earth Planets Space* **63**, 713 (2011). doi:10.5047/eps.2011.05.006

27. Y. Tanioka, K. Satake, Tsunami generation by horizontal displacement of ocean bottom. *Geophys. Res. Lett.* **23**, 861 (1996). doi:10.1029/96GL00736

28. M. Chlieh *et al*., Coseismic slip and afterslip of the great M-w 9.15 Sumatra-Andaman earthquake of 2004. *Bull. Seismol. Soc. Am.* **97**, (1A), S152 (2007). doi:10.1785/0120050631

29. C. DeMets, R. G. Gordon, D. F. Argus, Geologically current plate motions. *Geophys. J. Int.* **181**, 1 (2010). doi:10.1111/j.1365-246X.2009.04491.x

30. A. N. B. Poliakov, R. Dmowska, J. R. Rice, Dynamic shear rupture interactions with fault bends and off-axis secondary faulting. *J. Geophys. Res.* **107**, (B11), 2295 (2002). doi:10.1029/2001JB000572

31. L. Meng, J. P. Ampuero, A. Sladen, H. Rendon, High-resolution backprojection at regional distance: Application to the Haiti M7.0 earthquake and comparisons with finite source studies. *J. Geophys. Res.* **117**, (B4), B04313 (2012). doi:10.1029/2011JB008702

32. R. O. Schmidt, Multiple Emitter Location and Signal Parameter-Estimation. *IEEE Trans. Antenn. Propag.* **34**, 276 (1986). doi:10.1109/TAP.1986.1143830

33. P. Goldstein, R. J. Archuleta, Deterministic Frequency-Wave-Number Methods and Direct Measurements of Rupture Propagation during Earthquakes Using a Dense Array - Data-Analysis. *J. Geophys. Res.* **96**, (B4), 6187 (1991). doi:10.1029/90JB02472

34. D. J. Thomson, Spectrum Estimation and Harmonic-Analysis. *Proc. IEEE* **70**, 1055 (1982). doi:10.1109/PROC.1982.12433

35. S. Rost, C. Thomas, Array seismology: Methods and applications. *Rev. Geophys.* **40**, 1008 (2002). doi:10.1029/2000RG000100

36. J. A. Snoke, Traveltime Tables for IASP91 and AK135. *Seismol. Res. Lett.* **80**, 260 (2009). doi:10.1785/gssrl.80.2.260